ADVANCED FUNCTIONAL MATERIALS
www.afm-journal.de

Perovskite-Induced Ultrasensitive and Highly Stable Humidity Sensor Systems Prepared by Aerosol Deposition at Room Temperature

Myung-Yeon Cho, Sunghoon Kim, Ik-Soo Kim, Eun-Seong Kim, Zhi-Ji Wang, Nam-Young Kim, Sang-Wook Kim,* and Jong-Min Oh**

A new capacitive-type humidity sensor is proposed using novel materials and fabrication process for practical applications in sensitive environments and cost-effective functional devices that require ultrasensing performances. Metal halide perovskites ($CsPbBr_3$ and $CsPb_2Br_5$) combined with diverse ceramics (Al_2O_3, TiO_2, and $BaTiO_3$) are selected as sensing materials for the first time, and nanocomposite powders are deposited by aerosol deposition (AD) process. A state-of-the-art $CsPb_2Br_5/BaTiO_3$ nanocomposite humidity sensor prepared by AD process exhibits a significant increase in humidity sensing compared with $CsPbBr_3/Al_2O_3$ and $CsPbBr_3/TiO_2$ sensors. An outstanding humidity sensitivity (21426 pF RH%$^{-1}$) with superior linearity (0.991), fast response/recovery time (5 s), low hysteresis of 1.7%, and excellent stability in a wide range of relative humidity is obtained owing to a highly porous structure, effective charge separation, and water-resistant characteristics of $CsPb_2Br_5$. Notably, this unprecedented result is obtained via a simple one-step AD process within a few minutes at room temperature without any auxiliary treatment. The synergetic combination of AD technique and perovskite-based nanocomposite can be potentially applied toward the development of multifunctional sensing devices.

1. Introduction

Humidity sensing devices have attracted significant attention for their numerous potential applications such as structural health monitoring, precise control of living systems, hospital apparatus, and agricultural fields.[1–4] Recently, various transduction mechanisms and sensing materials for humidity sensors have been widely studied to provide high sensitivity, fast response/recovery time, excellent linearity, and low hysteresis by reading out electrical or optical signals (e.g., capacitance, resistance, photoluminescence, and gate effect in semiconductor devices).[5–10] In general, the sensitivity and response/recovery time have been considered the most important aspects of recent research involving humidity sensors.[11,12] In certain circumstances, it is extremely critical for such sensors to retain long-term stability and reliability, even under high-humidity environments.

Till date, significant effort has been made for the development of ceramic-based capacitive humidity sensors because they can achieve excellent relative humidity sensing performance over a wider range than resistive-type sensors.[13,14] The capacitive-type humidity sensing principle is fulfilled using the Grotthuss mechanism, which has been previously reported.[15,16] For highly sensitive ceramic-based sensors, there have been many studies over several decades using various processes, the fabrication of porous structures, and the incorporation of nanomaterials.[17–19] Despite their numerous advantages, including their outstanding resistance to physical and chemical attacks, long-term stability, and high sensitivity, certain challenges still remain for ceramic-based humidity sensors. This is because of the chemisorption of water molecules, as well as poor linearity and sensitivity over a wide humidity range, all of which limit their practical use in commercial humidity sensors.[20,21] Because of the above deficiencies, polymer-based humidity sensors are more widely used and studied compared to ceramic-based humidity sensors.[22,23] Additional challenges associated with ceramic-based humidity sensors are related to the conventional manufacturing processes. For instance, difficult fabrication methods or multistep processes are essentially required to create a layer-by-layer structure, which is generally complicated, non-eco-friendly, and time-consuming.[24–27] Such methods usually need a high-temperature and ultravacuum, electroplating, or a series of intermediate processes, which results in them

M.-Y. Cho, I.-S. Kim, Prof. J.-M. Oh
Department of Electronic Materials Engineering
Kwangwoon University
Seoul 01897, Republic of Korea
E-mail: jmOH@kw.ac.kr
S. Kim, Prof. S.-W. Kim
Nanomaterials Laboratory
Department of Molecular Science and Technology
Ajou University
Suwon 16499, Republic of Korea
E-mail: swkim@ajou.ac.kr
E.-S. Kim, Z.-J. Wang, Prof. N.-Y. Kim
RFIC Center
Department of Electronic Engineering
Kwangwoon University
Seoul 01897, Republic of Korea
E-mail: nykim@kw.ac.kr
The ORCID identification number(s) for the author(s) of this article can be found under https://doi.org/10.1002/adfm.201907449.

DOI: 10.1002/adfm.201907449

being unsuitable for application to commercial sensor products owing to high costs. Consequently, a simple and economical process at room temperature is important to the preparation of cost-effective as well as ultrasensitive sensors for wide commercialization. Furthermore, the integration of new materials is key to the development of novel humidity-sensing platforms with innovative electrical properties and sensing performances compared with existing device concepts.

Metal halide perovskites (MHPs) have superior optoelectrical properties that have attracted much attention in the field of optoelectronics, including solar cells, down-converting materials, light-emitting diodes, and photodetectors.[28–32] MHPs such as $CH_3NH_3PbI_{3-x}Cl_x$ and $CH_3NH_3PbBr_3$ have been shown to be sensitive to moisture exposure with increasing relative humidity (RH) using their photoluminescence intensity or resistance, resulting in an ultrasensitive performance.[33–35] Nevertheless, major problems involving halide perovskites were identified by the dissolution or chemical reaction with water molecules in humid environments. This inevitably degrades their reproducibility and stability as a long-term humidity sensor. Another issue is the long response and recovery times of ≈250 and 70 s, respectively, to reach 90 RH% from atmospheric equilibrium state,[35] which are not suitable for humidity sensing devices. To overcome stability and response/recovery issues caused by water–MHP reactions, a recent study proposed a $Cs_2BiAgBr_6$ material with outstanding stability in ambient environments.[36] Nevertheless, even though a stability below 70 RH% and a response/recovery time (1.78 s/0.45 s) were better than previous MHP humidity sensors, it still exhibited fluctuating signal values across the whole dynamic range for the duration of the stability test. Most importantly, the sensing performance exhibited considerably attenuated stability above 70 RH%. Therefore, the MHP would be considered a disposable sensor, and this is not preferable in humidity-sensing materials.

Alternatively, by considering the strong ionic nature of all inorganic MHPs (which has received little attention in MHP application fields), our study has demonstrated for the first time a novel capacitive-type humidity sensor that combines a cost-effective aerosol deposition (AD) process with MHP-based ceramic nanocomposite materials employed at room temperature to achieve excellent sensing performance and stability. We mainly utilized the high sensitivity of MHP to moisture as an effective polarization effect in a capacitive-type humidity sensor, expecting an excellent linearity and humidity detection in low as well as high humidity conditions, which is currently an important issue involving ceramic-based humidity sensors. Meanwhile, we also targeted highly enhanced stability by utilizing ceramic matrixes as a protector of MHPs at elevated humidity. Notably, the AD process is simpler, cost-effective, and has faster deposition time compared with RF sputtering, hydrothermal-electrochemical method, electrospinning, spin-coating, and ink-jet printing; the latter is one of the simplest processes in humidity sensor research.[37] The fundamental AD principle is explained by the fact that certain powders severely collide with target substrates and easily form well-adhered ceramic coating layers, generating a high bonding strength and fine nanocrystalline particles on the substrate.[38–40]

In our previous work, $CsPbBr_3/Al_2O_3$ nanocomposites were readily synthesized via the recrystallization of CsBr and $PbBr_2$ ionic salts in dimethyl sulfoxide (DMSO) using Al_2O_3 as a support, as shown in Figure S1 (Supporting Information).[28] Similarly, nanocomposite powders with cesium lead bromide (CPB) and the other ceramic materials were successfully synthesized, considering the dielectric properties of host materials, such as TiO_2 and $BaTiO_3$, for a capacitive-type humidity sensor. These nanocomposite powders afford a deposited layer with uniform CPB distribution on a glass substrate with platinum interdigital capacitor using the AD method without a post-annealing process. Herein, nanocomposite films with CPB embedded in ceramic matrices are fabricated at room temperature for novel sensing characteristics with ultrasensitivity, fast response/recovery time, and long-term stability. The ultimately fabricated humidity sensor exhibited a high sensitivity of 21 426.6 pF $RH\%^{-1}$, linearity of 0.991, hysteresis of 1.7%, and high stability. To the best of our knowledge, this device demonstrates the most sensitive, linear, and stable humidity sensor reported to date.

2. Results and Discussion

2.1. High Polarizable $CsPbBr_3$ Effect on Humidity Sensitivity

The fabrication steps of the humidity sensor are simplified in **Figure 1**. In the AD process, the nanocomposite powders loaded into the aerosol chamber were aerosolized by the injected gas flow. The transferred aerosols from the aerosol chamber to the nozzle were severely impacted with the predesigned interdigital circuits (IDCs) using 24 finger-type electrodes, which are located 5 mm away from the nozzle, simply forming a sensing film with good adhesion.[41] The sensing performance of nanocomposite films were evaluated by obtaining a capacitance recording every 10 s with an increase in relative humidity, keeping the AD-prepared device in the humidity chamber. The detailed deposition mechanism and measurement procedure are described in the Experimental Section in the Supporting Information.

First, the humidity sensing properties were characterized considering the effects of both the ceramic matrix and $CsPbBr_3$. **Figure 2**a,b shows the variation in capacitance with RH ranging from 25 to 95 RH% for Al_2O_3-based and TiO_2-based sensors. The humidity sensitivity of pristine Al_2O_3 and TiO_2 was 0.033 and 0.45 pF $RH\%^{-1}$, respectively, as derived from the commercial sensitivity equation in a capacitive-type humidity sensor, following $\Delta C/\Delta RH$ (where C is the capacitance and RH is the relative humidity). The sensitivity gap between the above two materials was more than tens times, even though they were equally manufactured in terms of process and experimental conditions, so this circumstance can be assumed to be because of their dissimilar physical properties and polarization effect. Generally, the sensitivity of capacitive-type humidity sensor mainly depends on the bare permittivity.[42] Al_2O_3 has low permittivity due to its weak polarizability through ionic and electronic polarization.[43] These two types of polarizations limit the achievement of high permittivity, as polarizability is very small in comparison to space charge and dipole polarization effect. In the present situations, pristine Al_2O_3 film therefore has no capacitance alteration, even though the relative humidity was

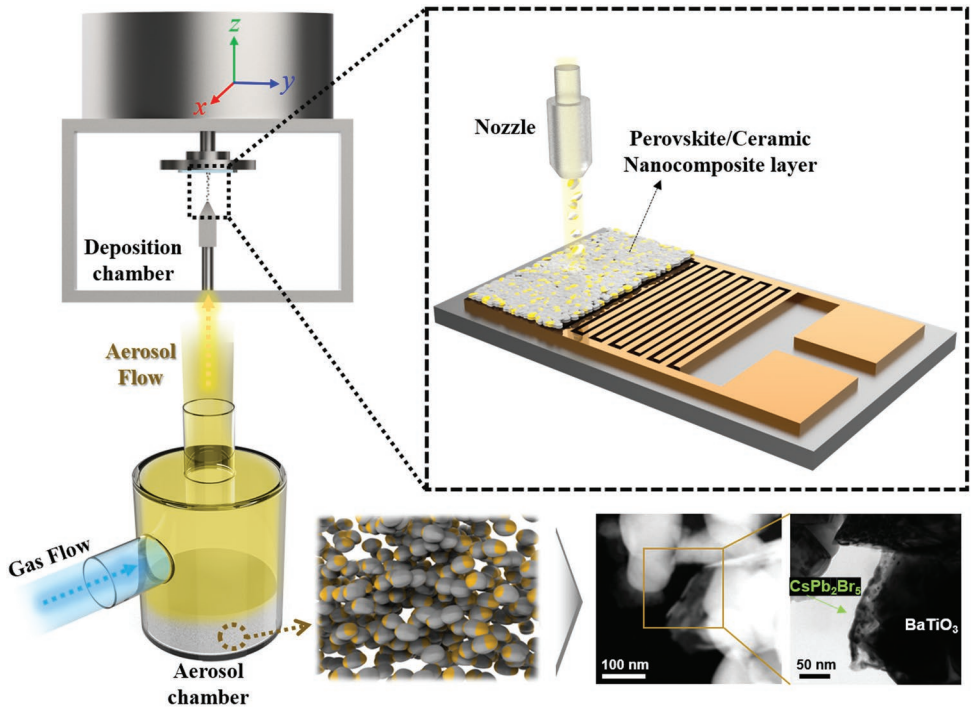

Figure 1. Schematic diagram of the aerosol deposition (AD) process flow for perovskite/ceramic nanocomposite films.

increased up to a very humid condition of 95 RH%. Even if the polarization of TiO_2 film was likewise composed of ionic and electronic polarization, as in Al_2O_3 film, it has a very strong polarizing power owing to the high charging effect of the Ti^{4+} cations, leading to an increase in the capacitance dynamic range with relative humidity.[44] Furthermore, Ti atoms are close to OH^- in water molecules, and it can be thought that the hydrophilic surface of TiO_2 film acts as a magnet for hydroxyl groups in water molecules.[45]

In comparison with pristine ceramic samples of Al_2O_3 and TiO_2 single layers, $CsPbBr_3$-impregnated humidity sensor shows remarkably high sensitivity. The humidity sensitivity of the $CsPbBr_3/Al_2O_3$ sensor was 1.75 pF RH%$^{-1}$, i.e., 53 times higher than that of Al_2O_3, while that of the $CsPbBr_3/TiO_2$ sensor was 2005.17 pF RH%$^{-1}$, i.e., ≈4500 times higher than that of pure TiO_2. Also, the results show that the sensitivities in low (L-sensitivity; 25–60 RH%) and high (H-sensitivity; 60–95 RH%) humidity conditions for $CsPbBr_3/Al_2O_3$ are 0.027 and 3.47 pF RH%$^{-1}$, respectively. Also, the L- and H-sensitivities of $CsPbBr_3/TiO_2$ are 0.428 and 4009.96 pF RH%$^{-1}$, respectively. This means that a $CsPbBr_3$ nanocrystal-embedded sensor can readily detect relatively low humidity values ranging from 25 to 60 RH%, consequently leading to higher capacitance variation compared to single ceramic layers. From this result, it is very important to highlight that the additional $CsPbBr_3$, which is distributed across entire regions (Figure S2, Supporting Information), have good potential to realize increased humidity sensitivity.

To better understand the effect of $CsPbBr_3$ based on the above unexpected results, the dielectric properties of the Al_2O_3-based humidity sensor were first analyzed. As shown in Figure 2c, the dielectric constant increases up to 160% for $CsPbBr_3/Al_2O_3$ compared with Al_2O_3 single layer. It is assumed that the increase in the dielectric constant by impregnated $CsPbBr_3$ in Al_2O_3 layer is associated with the intrinsic dielectric constant of $CsPbBr_3$ (20.5).[46] Unlike the case with only single-layer Al_2O_3 having weak polarization, such as ionic and electronic, the dielectric constant could be assisted by charge accumulation at the ceramic interface owing to the AC electric field. This observation is somewhat verified based on a trend line analysis, which means that the permittivity slope as a function of frequency from 200 Hz to 1 MHz slightly decreased in the case of $CsPbBr_3/Al_2O_3$ nanocomposite films, while the slope for the Al_2O_3 films did not vary with frequency. However, although it was clearly confirmed that the $CsPbBr_3$ effect from the humidity sensitivity was in good agreement with permittivity data, the permittivity of $CsPbBr_3/TiO_2$ showed a more dramatic impact, as shown in Figure 2d.

The aerosol-deposited TiO_2 single layer had a permittivity value of only ≈35 at 200 Hz, but this was higher than the Al_2O_3 film, whereas the permittivity of the $CsPbBr_3/TiO_2$ layer was markedly increased by more than 285%. Note that the permittivity value of the $CsPbBr_3/TiO_2$ layer rapidly decreased up to 45 at 1 MHz depending on the frequency. To date, such an unprecedented phenomenon with a substantial polarization effect in the low frequency range has not been reported in AD studies based on dielectric materials, indicating that our proposed model retains a sizable polarization effect. This result can be ascribed to the interfacial polarization effect of the presence of $CsPbBr_3$ nanocrystals, but it also implies a different polarization mechanism besides $CsPbBr_3/Al_2O_3$. Provided that the AC electrical field is applied in ceramic-$CsPbBr_3$ nanocomposite films, each ionic element, i.e., Cs^+, Pb^{4+} (or Pb^{4-}), and Br^-, plays a role in charge separation, moving in the grain

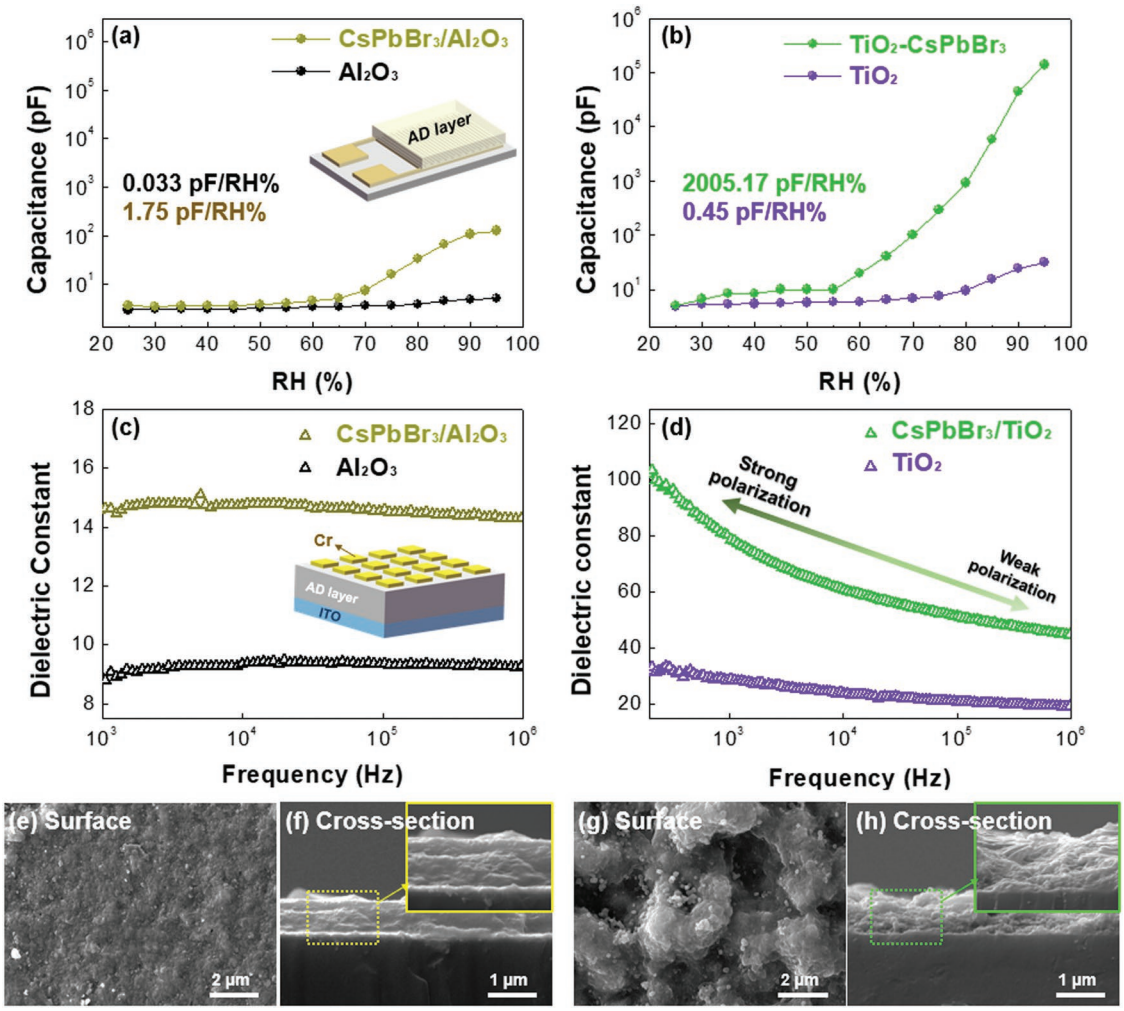

Figure 2. Capacitance variation with different RH values ranging from 25 to 95 RH% for a) Al_2O_3 and $CsPbBr_3/Al_2O_3$, and b) TiO_2 and $CsPbBr_3/TiO_2$ films. Dielectric constant of c) Al_2O_3 and $CsPbBr_3/Al_2O_3$, and d) TiO_2 and $CsPbBr_3/TiO_2$ layers with metal–insulator–metal structure. e,f) SEM images of the surface and cross-sectional microstructures of $CsPbBr_3/Al_2O_3$. g,h) SEM images of the surface and cross-sectional microstructures of $CsPbBr_3/TiO_2$. The insets of SEM images for (f) and (h) show the magnified area of cross-section of each film.

boundaries or space regions. Meanwhile, unbound electrons and thus formed atomic ions can help the polarization effect, leading to a higher permittivity.

Figure 2e–h shows the cross-section of $CsPbBr_3/Al_2O_3$ and $CsPbBr_3/TiO_2$ films, as observed from magnified SEM images. Both films exhibit well-adhered structures formed by the physical collision of particles on substrates, and is consistent with previous observations for AD process. However, Al_2O_3, which is known as a high-hardness ceramic, facilitates more hard coating layers during physical collision than TiO_2 particles.[47] Unfortunately, the presence of an extremely dense coating layer is regarded as an undesirable characteristic for humidity sensors because it negatively restricts the diffusion of water molecules into the inner structure. This interpretation can be validated scientifically in that the absorption of water molecules can effectively enhance the capacitance in the nanocrystalline layer owing to the high permittivity of water (≈81) as well as the continuous accumulation of water ions, such as O^{2-}, OH^-, and H_3O^+, which flow from the porous surface.[48] Eventually, this water-induced behavior causes space charge polarization, which is a major factor that contributes to an increase in capacitance. Therefore, it is difficult for a tightly clogged Al_2O_3 film to accept water molecules from even the top surface to the bottom layer, while only highly humid states allow the slight flow of water in densely formed layer. However, the capacitance of the TiO_2 coating layer can be easily increased by a relatively nondense microstructure and higher polarization effect.

Therefore, one possible explanation for the difference in interfacial polarization effects, or the frequency dependence of permittivity, between Al_2O_3-based and TiO_2-based sensors can be attributed to the structural properties. In other words, when ceramic-$CsPbBr_3$ films are in continuous contact with humid environment, some water molecules significantly contribute toward activating disequilibrium states in the internal structure due to the combination of water conductivity and conducting electrons, which effectively enhance the capacitance. Consequently, the relatively nondense $CsPbBr_3/TiO_2$ can easily absorb the water molecules, and also support the charge separation

through grain boundaries due to low hardness, leading to high variations in capacitance.

2.2. Role of Morphological Structure for Humidity Sensitivity

High surface-to-volume ratio is a well-known factor in improving the humidity sensing performance.[49–51] In addition, most previous studies on the humidity sensing performance of humidity sensors also focused largely on the porosity formation, such as the pore size or shape.[52–57] As a reliable hypothesis, the $CsPbBr_3/TiO_2$ layer can be expected to have an etching effect on its interior and exterior by water treatment owing to the ionic bonding character of MHP. It is possible to result in a $CsPbBr_3/TiO_2$ layer with a high surface-to-volume ratio, which can lead to a superior humidity sensitivity.

To clearly understand the effect of impregnated $CsPbBr_3$ in the TiO_2 matrix on the sensitivity, and more importantly, to simultaneously compare the $CsPbBr_3$ versus porous effect, we artificially constructed porous $CsPbBr_3/TiO_2$ nanocomposite layers by using water-soaking treatment with ultrasonification for 20 min to cause the liquid to sufficiently penetrate the film, as shown in **Figure 3**a. After preparing a series of TiO_2-based samples (pristine TiO_2, $CsPbBr_3/TiO_2$, and water-treated $CsPbBr_3/TiO_2$), a green emission of water-treated $CsPbBr_3/TiO_2$ under ultraviolet (UV) illumination was more weakened compared to the pure $CsPbBr_3/TiO_2$ nanocomposite layer (Figure 3b). The validated reason is considered to be that Cs, Pb, and Br elements were definitely reduced compared to pure $CsPbBr_3/TiO_2$ nanocomposite layers, but a few $CsPbBr_3$-related elements still remained, as shown in Figure S3 in the Supporting Information. This may have been due to their trapping conformation owing to the presence of some robustly combined ceramic particles.

Accordingly, variation in the surface and inner microstructure is observed after water soaking. As already anticipated, the surface of water-treated $CsPbBr_3/TiO_2$ nanocomposite layer displays a number of potholes by dissolving a part of $CsPbBr_3$ nanocrystal (Figure 3c), while that of $CsPbBr_3/Al_2O_3$ nanocomposite layer shows a highly dense formation as well as no CPB

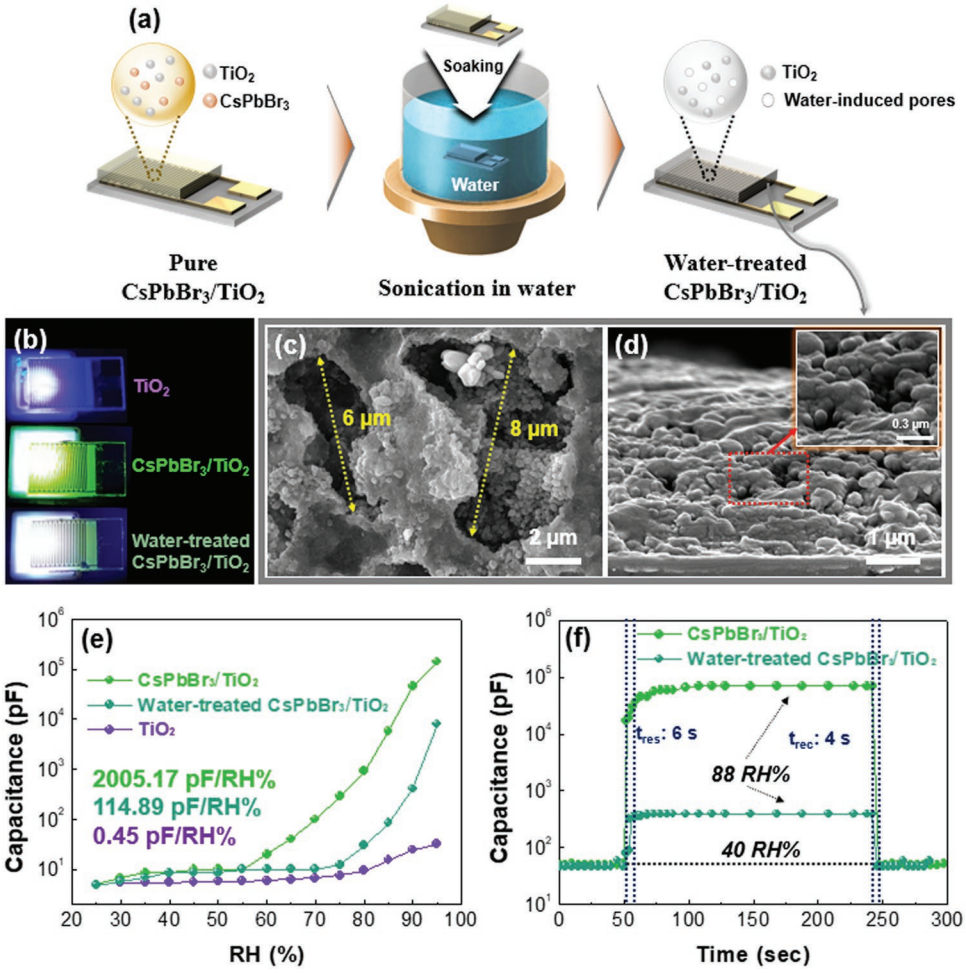

Figure 3. a) Schematic illustration of the water treatment process for $CsPbBr_3/TiO_2$ nanocomposite layers. b) Photoluminescence of TiO_2, $CsPbBr_3/TiO_2$, and water-treated $CsPbBr_3/TiO_2$ UV irradiation. c) Surface and d) cross-sectional morphologies of water-treated $CsPbBr_3/TiO_2$ samples. e) Variation of capacitance with different RH values and corresponding sensitivity of the three types of TiO_2-based samples. f) Response and recovery time analysis extracted from the sudden RH change from atmospheric condition (≈40 RH%) to high humidity state (≈88 RH%) for $CsPbBr_3/TiO_2$ and water-treated $CsPbBr_3/TiO_2$ samples.

elimination even after water soaking procedure (Figure S4, Supporting Information). A highly porous structure is confirmed in the cross-sectional micrograph (Figure 3d) of water-treated $CsPbBr_3/TiO_2$ layer against $CsPbBr_3/TiO_2$. Owing to the electron-permeable structure, dielectric properties including dielectric constant, impedance, and phase cannot be derived during impedance analysis by the electrical conduction path via several defects or wide grain boundaries in the surrounding dielectric region even under atmospheric humidity (Figure S5, Supporting Information). Such a phenomenon contributes to the highest surface area over excessive altitude variations among three samples (Figures S6 and S7, Supporting Information), allowing the water molecules to easily infiltrate into the internal structure due to numerous pores.[58]

In order to evaluate the effect of water-treated $CsPbBr_3/TiO_2$ on ultimate sensing performances, the humidity-sensing capabilities for three samples were evaluated at RH values ranging from 25 to 95 RH%, as shown in Figure 3e. The humidity sensitivity of water-induced $CsPbBr_3/TiO_2$ is ≈114.89 pF RH%$^{-1}$, which reduces by at least 17 times. The response/recovery time (t_{res}/t_{rec}) of this layer was 6 and 4 s, respectively, with a good result and an almost 100% reversibility (Figure 3f). The calibration of the response/recovery time was performed inside a chamber by controlling the RH value, which could be varied from 40% to 88% while conducting the capacitance measurement in real time. The response time is defined as the time corresponding to 90% of ΔC_{res} ($\Delta C_{res} = C1_{A88\%} - C1_{A40\%}$, where $C1_{A88\%}$ and $C1_{A40\%}$ are the average capacitances at 88 and 40 RH%, respectively).[36] Similarly, the recovery time is defined as the time taken to attain 90% of ΔC_{rec} ($\Delta C_{rec} = C_{88\%} - C2_{A40\%}$, where $C_{88\%}$ is the capacitance at 88 RH% and $C2_{A40\%}$ is the average capacitance at 40 RH%, respectively).

To further investigate the perovskite effect on sensing characteristics, all perovskite elements such as Cs, Pb, and Br were removed by soaking in DMSO and dimethylformamide (DMF) mixed solvent (9:1) for 1 h with ultrasonification. Consequently, as shown in Figure S8 in the Supporting Information, the green emission completely disappears compared with water-treated $CsPbBr_3/TiO_2$ layer due to substantial interaction between Pb^{2+} and Cs^+ ions with DMSO and DMF mixed solvent, showing porous inner structure.[59] Interestingly, the markedly porous structure obtained from the above procedure had a completely lowered sensitivity at about 1.35 pF RH%$^{-1}$ in Figure S9a. Although the DMSO/DMF-treated $CsPbBr_3/TiO_2$ layer involved very small quantities of perovskite concentrations (Figure S9b, Supporting Information), the interfacial polarization effect caused by the spatial charge separation of $CsPbBr_3$ would not be serve the remarkable factors for increasing humidity sensitivity; instead, the DMSO/DMF-treated porous structure would rather devote its ideal capillary water condensation by a great number of open-pore distributions, which may normally be considered to be one of the primary factors of the humidity sensitivity. Therefore, comparing four types of TiO_2-based humidity sensors, it is confirmed that halide perovskite nanocrystals embedded in TiO_2 matrices play a key role in humidity sensitivity performance, based on a large gap in the humidity sensitivity between with/dissolved $CsPbBr_3$, rather than humidity-induced local interfacial polarization or good water-permeable layer in mesoporous structure.

However, one major problem was observed with $CsPbBr_3/TiO_2$ despite its higher sensitivity compared to others. We observed that the capacitance of $CsPbBr_3/TiO_2$ steadily decreased while the humidity was maintained at 90 RH%, whereas the water-treated $CsPbBr_3/TiO_2$ remained relatively unchanged, even under high-humidity conditions (**Figure 4**a). To understand this, the crystalline structures were characterized by XRD analysis to investigate changes in the embedded $CsPbBr_3$ nanocrystals in the TiO_2 matrix with and without water treatment. Intriguingly, XRD patterns of water-treated nanocomposite films presented some phase transition from cubic $CsPbBr_3$ to tetragonal $CsPb_2Br_5$ (Figure 4b). This phenomenon is typically generated by the water-treated irreversible decomposition to $PbBr_2$, Cs^+(aq), and Br^-(aq) owing to the strong ionic nature of $CsPbBr_3$. Subsequently, Cs^+ removal is accelerated and $PbBr_2$ can react with residual $CsPbBr_3$, forming $CsPb_2Br_5$.[60] Accordingly, some of the embedded $CsPbBr_3$ phase in $CsPbBr_3/TiO_2$ layer is transformed into $CsPb_2Br_5$ during the aging test at 90 RH%, whereas the residual $CsPb_2Br_5$ in water-treated $CsPbBr_3/TiO_2$ undergoes no phase transition, as shown in Figure 4c. Based on the stability results, in spite of the significant assistance in the humidity sensitivity via $CsPbBr_3$, MHP continues to have significant issues, including the rapid abscission of some ions during phase transitions once there is contact with moisture, even if $CsPbBr_3$ molecules are effectively embedded in ceramic grains. It should also be noted that $CsPb_2Br_5$ in the water-treated sample also significantly increased the sensitivity as well as the stability when compared to DMSO/DMF-treated $CsPbBr_3/TiO_2$, which has almost the same structure and rare CPB amount in Figure S9b in the Supporting Information.

Therefore, it can be concluded that the sensing performance and reliability of CPB/ceramic composite films for a humidity sensor are predominantly affected by three factors: 1) host ceramic matrix with high permittivity, 2) significant interfacial polarization effect and high stability of tetragonal $CsPb_2Br_5$ crystalline phase with a gradual increase in RH, and 3) the buildup of inner porous structure, which is beneficial for large water absorption.

2.3. Supersensitive and Highly Stable $CsPb_2Br_5/BaTiO_3$ Nanocomposite

Based on these highly sensitive and rapidly responsive MHP-based humidity sensors prepared by room-temperature AD process, state-of-the-art $CsPb_2Br_5/BaTiO_3$ nanocomposite layers were fabricated for effective moisture detection in dynamic RH ranges, focusing on the optimization of three factors: the ferroelectric ceramic matrix (with dipole, ionic, and electronic polarizations), $CsPb_2Br_5$-based enhanced stability and massive charge separation action, and porous structures for water-permeable layer. First, the $CsPb_2Br_5/BaTiO_3$ nanocomposite powder was successfully obtained; the synthesis procedure is described in the Experimental Section in the Supporting Information.

Figure 5a shows the humidity sensitivity aligning with two $BaTiO_3$-based humidity sensors both with and without embedded $CsPb_2Br_5$ nanocrystals ranging from 25 to 95 RH%. For the sensitivity, the capacitance was measured every 10 s

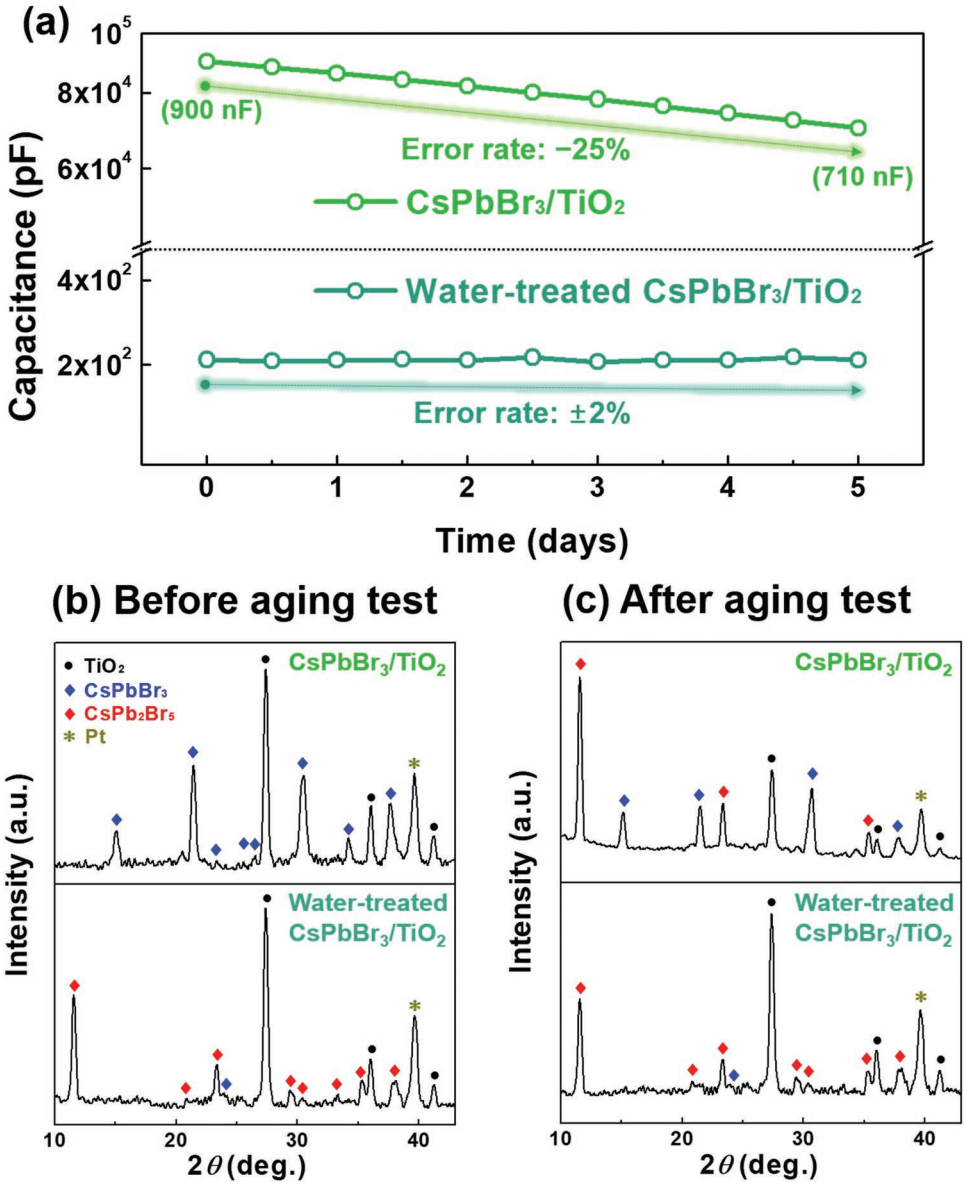

Figure 4. a) Aging tests of pure and water-treated $CsPbBr_3/TiO_2$ humidity sensors under 90 RH% for five days. XRD analysis of two types of $CsPbBr_3/TiO_2$ b) before and c) after high humidity test at 90 RH%.

with an increase of RHs in Figure S10 in the Supporting Information. The data show outstanding performance results; the humidity sensitivity of $BaTiO_3$ single layer is only 1.39 pF RH%$^{-1}$ with a relatively low gap between $C_{25\ RH\%}$ and $C_{95\ RH\%}$, while that of $CsPb_2Br_5/BaTiO_3$ has a high sensitivity value of 21 426.6 pF RH%$^{-1}$. In addition, this susceptible capacitance changes with different RH values, and also showed a superior linear configuration (linearity (*L*): 0.991) in the overall ranges, displaying the much higher capacitance increment among our all samples, while a single $BaTiO_3$ layer was very insensitive (*L*: 0.493) below 70 RH%. To the best of our knowledge, these variations of 20 000 orders of magnitude in the capacitance signal, which is obtained by varying the RHs from the dehydrated state to seriously humid conditions, is in line with the best data recently reported on $BaTiO_3$-based capacitive sensors having values below 5000 pF RH%$^{-1}$, as well as on whole ceramic-based capacitive sensors (Table S1, Supporting Information).[61–68] Moreover, an unprecedented value of 7499 300% is obtained based on the calculation: $C_{95\ RH\%} - C_{25\ RH\%}/C_{25\ RH\%} \times 100\%$, which is the second highest value ever reported for the existing humidity sensors. Remarkably, the hysteresis value reaches 1.7% (Figure 5b). The response/recovery time of $CsPb_2Br_5/BaTiO_3$ sample is ≈5 s, which is greater than that of most $BaTiO_3$-based sensors, as shown in Figure 5c. Aside from the above sensing performances, the moisture stability of $CsPb_2Br_5/BaTiO_3$ layers was confirmed by carrying out an aging test from 40 to 90 RH%, preserving each humidity level for 5 days, as shown in Figure 5d. Unlike $CsPbBr_3$-based humidity sensors, $CsPb_2Br_5/BaTiO_3$ layer shows almost no attenuation at all humidity levels, which is the best stability ever reported

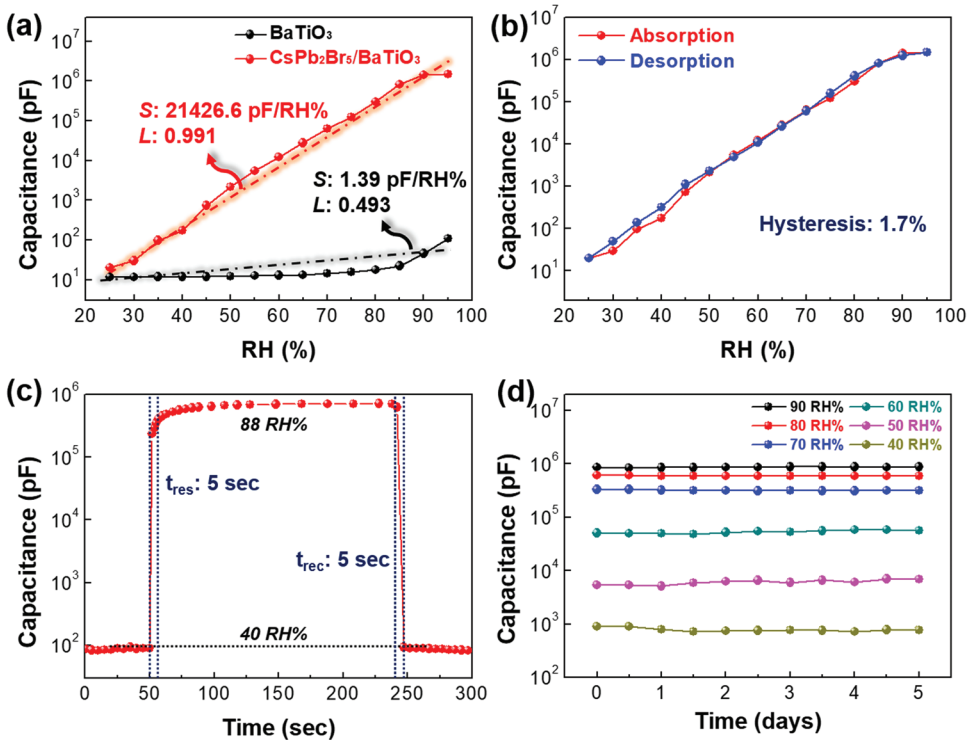

Figure 5. a) Humidity sensor performance of $CsPb_2Br_5/BaTiO_3$ and $BaTiO_3$ (capacitance vs RH; *S*: sensitivity; *L*: linearity). b) Hysteresis result for $CsPb_2Br_5/BaTiO_3$ nanocomposite layer from 25 to 95 RH% c) Response and recovery tests of $CsPb_2Br_5/BaTiO_3$ humidity sensor based on sudden humidity change from 40 to 88 RH%. d) Stability of $CsPb_2Br_5/BaTiO_3$ layers in diverse humid environments (40, 50, 60, 70, 80, and 90 RH%).

among MHP-based humidity sensors. The high stability can be attributed to the following factors: 1) $CsPb_2Br_5$ has very low solubility and exhibits no phase transition,[69–71] and 2) $BaTiO_3$ acts as a protective framework for $CsPb_2Br_5$. Consequently, $CsPb_2Br_5$ nanocrystals are adsorbed and dispersed in the nanocomposite layers, showing no phase transformation and no reduction in $CsPb_2Br_5$ amount, which demonstrates that this water-resistant MHP is immune to humid conditions and is beneficial in comparison to previous MHP-based humidity sensors (Figure S11, Supporting Information). Based on this high stability, $CsPb_2Br_5/BaTiO_3$ layered sensors show excellent repeatability, as shown in Figure S12 in the Supporting Information.

The novel humidity sensing mechanism of $CsPb_2Br_5/BaTiO_3$ nanocomposite layer includes (**Figure 6**a) 1) a 3D porous structure, 2) ideal capillary structure to allow ready diffusion of the water molecules, 3) fast response through strong affinity between moisture and perovskite, and 4) substantial polarization effect by the migration of perovskite ions and unbound electrons under electric field. As shown in Figure 6b, the dielectric constant of $CsPb_2Br_5/BaTiO_3$ layers is ≈45 at ≈200 Hz and continuously decreases to a value that is four times lower than the original value with an increase in frequency of up to 1 MHz. Such a change in the dielectric constant clearly indicates that the beneficial polarization ability is in good agreement with the high sensitivity as this fundamental origin is totally dependent on the $CsPb_2Br_5$, which caused dielectrically disequilibrium states of the nanocomposite structure. The slope for dielectric constant as a function of frequency reduces, indicating that $CsPb_2Br_5$ nanocrystals embedded in the $BaTiO_3$ matrix effectively result in the polarization effect. As $CsPbBr_3/TiO_2$ shows a remarkably enhanced sensitivity in comparison to a single TiO_2 matrix layer, the mechanism for $CsPb_2Br_5/BaTiO_3$ possibly involves $CsPb_2Br_5$, which assists in charge separation among spatial inner defects or grain boundaries. This phenomenon allows a rapid increase in capacitance with an increase in RH. In some cases, the perovskite lattice can interact with the polar water molecules during humidification due to the formation of strong hydrogen bonds between water and the halide (bromide) lattice.[34]

Secondly, as shown in Figure 6c, a clearly porous structure was readily obtained without any dissolution treatment, whereas only a $BaTiO_3$ layer presented a highly dense structure with few pores (Figure S13, Supporting Information). The reason why the porous and capillary-type structure is important is that a lot of absorbed water molecules contact with $CsPb_2Br_5$ so that this nanocomposite layer can provide a stronger polarization effect even at low humidities. This result is primarily ascribed to a wide disparity in kinetic energies of the physical properties of raw powder during the AD process. As ceramic powders are a type of hard materials, which encounter a cumulative hammering effect, these can simultaneously decrease the grain and pore sizes, restricting the sensing ability particularly at low RH values. Although high impact energies are desirable for the fabrication of a densely packed structure with surface lubricity, the single ceramic structure is considerably hard, and it not only accepts the water molecules in the closed surface area but also accumulates them in the internal structure

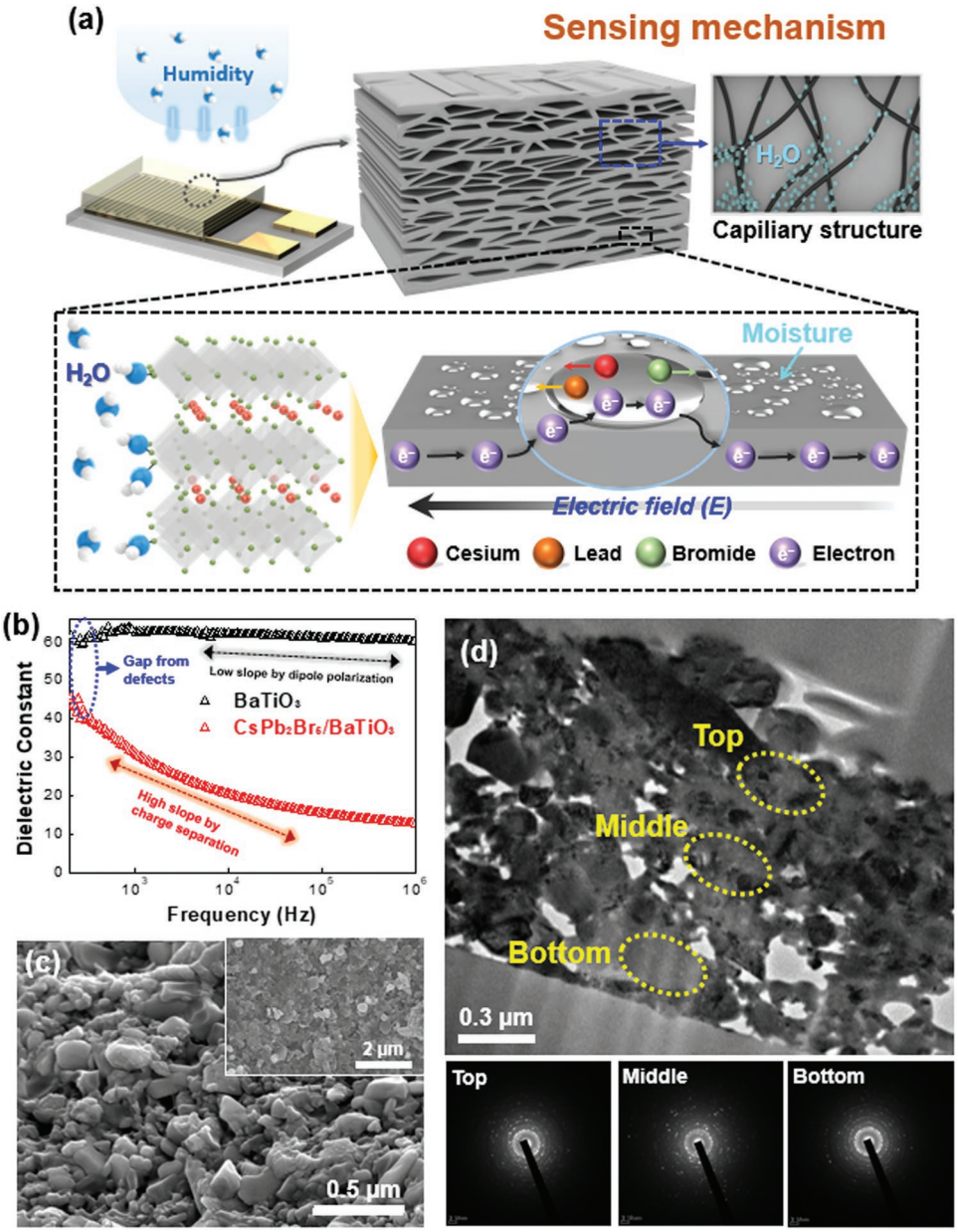

Figure 6. a) Schematic of the humidity sensing mechanism of the $CsPb_2Br_5/BaTiO_3$ sensor. b) Dielectric constant as a function of frequency (from 200 Hz to 1 MHz) for $BaTiO_3$ and $CsPb_2Br_5/BaTiO_3$ layers. c) Cross-sectional SEM images of porous $CsPb_2Br_5/BaTiO_3$ layer (the inset shows its surface image). d) TEM image of $CsPb_2Br_5/BaTiO_3$ layers with a representative SAED pattern of top, middle, and bottom regions.

owing to very few and small pore distributions. In contrast, a number of relatively soft $CsPb_2Br_5$ molecules surrounding $BaTiO_3$ can relieve the impact energy during collision with the substrate, resulting in a large-grained configuration as well as a porous structure due to the noncompact particle-to-particle combination. Notably, this porous $CsPb_2Br_5/BaTiO_3$ structure was formed with N_2 carrier gas, which prevents the formation of a dense structure because of low kinetic energy, whereas $CsPbBr_3/TiO_2$ nanocomposite layers were fabricated with He gas which provides a more high-impact energy to the predeposited films during collision.[40] Therefore, $CsPb_2Br_5/BaTiO_3$ has an ideal capillary structure, which allows the deep penetration of water molecules (Figure 6d), whereas AD-prepared $BaTiO_3$ humidity sensor had a transitional dense structure from top to bottom region due to the hammering effect.[72,73] Accordingly, all selected area electron diffraction (SAED) patterns for the three regions (top, middle, and bottom of the nanocomposite layer) show a more intense and asymmetric diffraction, indicating that the large-size crystallites are nonuniformly distributed.[74] As shown in Figure S14 in the Supporting Information, atomic force microscopy (AFM) results prove that the more roughened $CsPb_2Br_5/BaTiO_3$ has a large surface area ratio of ≈132 μm^2, assuming that the flat surface has an area of 100 μm^2, while $BaTiO_3$ layer has a surface area 112 μm^2 in

the local regions. The $CsPb_2Br_5/BaTiO_3$ surface also exhibits highly sunken parts of up to 500 nm depth in the entire region, presenting extreme surface altitude variations which are beneficial for water-permeable structures. It should be noted that this novel sensing film was fabricated using only the AD process at room temperature without any treatments as well as subsidiary layers with auxiliary processes.

3. Conclusion

In summary, we have introduced a new type of capacitive-type humidity sensor based on cesium-lead-halide perovskites and ferroelectric heterocomplex structures together with a very efficient AD method. As a first step to establishing the undefined feasibility of the CPB impact on the humidity sensing capability, a comparative study was carried out between Al_2O_3 and $CsPbBr_3/Al_2O_3$, simultaneously dealing with TiO_2-based sensors by concentrating on the CPB-induced polarization effect and structural properties. The water-treated $CsPbBr_3/TiO_2$ layer also exhibited very high sensitivity, but lower than that of $CsPbBr_3/TiO_2$, which could possibly originate from the residual $CsPb_2Br_5$ instead of the porous structure. Synthetically, an ultimate nanocomposite layer was fabricated using $BaTiO_3$ and $CsPb_2Br_5$ to achieve high sensitivity, quick response/recovery time, and stability. The subsequent result clearly showed that compared with previous $BaTiO_3$-based sensors, $CsPb_2Br_5/BaTiO_3$ nanocomposite layers had extremely high sensitivity, low hysteresis, fast response/recovery time, and long-term stability even under high humidity environments. Notably, this film was fabricated only using the AD process at room temperature without any auxiliary treatments. This unprecedented outcome with highly cost-effective and unique AD characteristics may be constructed by employing various desired complex features and the synergetic effect in the humidity sensors.

This novel approach and properties were confirmed based on the utilization of a ferroelectric ceramic, the desirable polarization effect of $CsPb_2Br_5$, porous structure, open-pore distributions, and high surface area. The current efforts will provide the pathway for new visions of multifunctional sensing devices and future commercial markets by employing simple and cost-effective manufacturing processes.

4. Experimental Section

Synthesis of $CsPbBr_3/Al_2O_3$ Nanocomposite Powders: CsBr (6.7 g, 22.1 mmol, Alfa Aesar, Haverhill, Massachusetts, USA) and $PbBr_2$ (8.1 g, 22.1 mmol, Sigma-Aldrich, St. Louis, Missouri, USA) were vigorously stirred and completely dissolved in 200 mL of DMSO at 100 °C for a few minutes. This solution was transferred to a planetary mixer, into which α-Al_2O_3 powder (D50, 520 nm, 100 g, Showa denco, Tokyo, Japan) was poured. This slurry was heated at 160 °C to evaporate DMSO until it became a paste, which was further dried at 160 °C in a dry oven for 24 h. The obtained solidified powder was grinded using a mortar for ≈30 min. To demonstrate PL, this yellowish powder was heat-treated at 500 °C for 1 h (heating rate: 5 °C min^{-1}). Finally, the product, a yellowish $CsPbBr_3/Al_3O_3$ nanocomposite powder, was obtained.

Synthesis of $CsPbBr_3/TiO_2$ and $CsPb_2Br_5/BaTiO_3$ Nanocomposite Powders: CsBr (6.7 g, 22.1 mmol) and $PbBr_2$ (8.1 g, 22.1 mmol) were vigorously stirred and completely dissolved in 200 mL of DMSO at 100 °C for a few minutes. This solution was transferred to a planetary mixer, into which TiO_2 (Sigma-Aldrich) or $BaTiO_3$ powder (D50, 570 nm, 100 g, SBT-045B, Samsung Fine Chemical, Ulsan, South Korea) was poured. This slurry was heated at 160 °C to evaporate DMSO until it became a paste, which was further dried at 160 °C in a dry oven for 48 h. The obtained solidified powder was grinded using a mortar for ≈30 min. Finally, $CsPbBr_3/TiO_2$ and $CsPb_2Br_5/BaTiO_3$ nanocomposite powders were obtained.

Humidity Sensor Fabrication: To deposit the ceramic–metal halide perovskite nanocomposite films, aerosol deposition (AD) process based on room temperature impact consolidation was employed. Ceramic–metal perovskite nanocomposite powder was stored in a dry oven at ≈100 °C for minimum 24 h to remove residual moisture or aggregates. After percolating them with a fine sieve net, these powders were placed in an aerosol chamber and propelled to a deposition chamber by injecting a nitrogen carrier gas (purity: 99.99%) into the powder. Before the deposition, all interiors including aerosol as well as deposition chambers were pre-evacuated up to ≈3.2 Torr by vacuum pump systems to mitigate the deceleration of sprayed aerosols from the nozzle. In the actual deposition step, the blown aerosol from carrier gas was transported through a Teflon tube to a stainless-steel nozzle with an orifice size of 0.4 × 10.0 cm^2. Subsequently, these accelerated aerosols impinged strongly with the substrate located 5 mm away from the nozzle. Through strong particle-to-particle and particle-to-substrate cohesions, AD-prepared nanocomposite films were obtained. Detailed experimental conditions are listed in Table S2 in the Supporting Information.

Humidity Sensing Measurement: An impedance analyzer (4192A, Agilent Co. Ltd., Santa Clara, California, USA) was utilized to measure the variation in capacitance with relative humidity. The frequency and applied voltage were fixed to 100 Hz and 1 V, respectively, to effectively identify the interfacial polarization effect of water molecules as well as halide perovskite in ceramic matrix. All humidity sensors were tested in a humidity chamber (TH-ME-025, Jeiotech Co. Ltd., Seoul, South Korea), which was connected with an impedance analyzer, at 25–95 RH%. This interlocking system allows automatic measurement of capacitance at least every second. The capacitance was measured for each 5 RH% increase (25, 30, 35, ..., 95 RH%). In this range, after retaining the specific humidity for ≈10 min, the average capacitance for 10 min was determined. The sensitivity was calculated by $\Delta C/\Delta RH$, as typically used in commercial studies. The response/recovery times were obtained by a drastic humidity change from the atmospheric humidity (≈40 RH%) to that inside a chamber, which was maintained at ≈88 RH%. The aging test was performed in diverse humidity environments (40, 50, 60, 70, 80, and 90 RH%) for five days together with continual capacitance recording by an impedance analyzer.

Sensor Characterization: Scanning transmission electron microscopy (STEM, JEM-2100F, JEOL, Tokyo, Japan) was used to observe the inner structure of $CsPb_2Br_5/BaTiO_3$ nanocomposite layer and the elemental distribution of nanocomposite powders at a beam energy of 300 keV. AFM (XE150, PSIA, Suwon, South Korea) with noncontact mode was employed to analyze the surface topography and average roughness. These AFM data were analyzed using XEI software program (Park Systems Corp., Suwon, South Korea) for presenting top and 3D morphological views. The surface and microstructures of the samples were observed through field-emission scanning electron microscopy (FE-SEM, S-470, Hitachi Ltd., Tokyo, Japan) at 10 kV. XRD (Ultimate III diffractometer, Rigaku Corp., Tokyo, Japan) was utilized to evaluate the crystallinity and phase transformation of the samples with Cu Kα radiation of 1.5406 Å over a 2θ range of 10°–50°. In this measurement, energy-dispersive X-ray spectroscopy (EDS) was simultaneously performed for determining the elemental distributions. The dielectric properties of the samples were measured by an impedance analyzer (HP-4194A, Agilent Technologies, Inc., Santa Clara, California, USA) at 1 V.

Supporting Information

Supporting Information is available from the Wiley Online Library or from the author.

Acknowledgements

This present research was conducted by the Research Grant of Kwangwoon University in 2019. This research was also supported by the Basic Science Research Program through the National Research Foundation of Korea (NRF) funded by the Ministry of Science, ICT and Future Planning (Nos. 2017R1C1B5017013 and 2014R1A5A1009799) and the Ministry of Education (No. 2018R1A6A1A03025242). Additionally, this work was assisted by Nano Material Technology Development Program through the National Research Foundation of Korea (NRF) funded by the Ministry of Science, ICT and Future Planning (2009-0082580). And, this work was supported by the Korea Institute of Energy Technology Evaluation and Planning (KETEP) under the Ministry of Trade, Industry & Energy (MOTIE) (No. 20173010013200).

Conflict of Interest

The authors declare no conflict of interest.

Author Contributions

M.-Y.C. and S.K. contributed equally to this work.

Keywords

aerosol deposition, humidity sensitivity, humidity sensors, perovskite/ceramic nanocomposites, stability

Received: September 9, 2019
Revised: October 25, 2019
Published online:

[1] M. A. Squillaci, L. Ferlauto, Y. Zagranyarski, S. Milita, K. Müllen, P. Samorì, *Adv. Mater.* **2015**, *27*, 3170.
[2] U. Mogera, A. A. Sagade, S. J. George, G. U. Kulkarni, *Sci. Rep.* **2014**, *4*, 4103.
[3] J. Chu, X. Peng, P. Feng, Y. Sheng, J. Zhang, *Sens. Actuators, B* **2013**, *178*, 508.
[4] Y. Wang, R. W. Besant, C. J. Simonson, W. Shang, *Sens. Actuators, B* **2006**, *115*, 93.
[5] N. A. Roslan, A. Abu Bakar, T. M. Bawazeer, M. S. Alsoufi, N. Alsenany, W. H. Abdul Majid, A. Supangat, *Sens. Actuators, B* **2019**, *279*, 148.
[6] K. Szendrei-Temesi, O. Sanchez-Sobrado, S. B. Betzler, K. M. Durner, T. Holzmann, B. V. Lotsch, *Adv. Funct. Mater.* **2018**, *28*, 1705740.
[7] P. Yasaei, A. Behranginia, T. Foroozan, M. Asadi, K. Kim, F. Khalili-Araghi, A. Salehi-Khojin, *ACS Nano* **2015**, *9*, 9898.
[8] J. Zhao, N. Li, H. Yu, Z. Wei, M. Liao, P. Chen, S. Wang, D. Shi, Q. Sun, G. Zhang, *Adv. Mater.* **2017**, *29*, 1702076.
[9] D. Zhang, Y. Sun, P. Li, Y. Zhang, *ACS Appl. Mater. Interfaces* **2016**, *8*, 14142.
[10] D. Zhang, H. Chang, P. Li, R. Liu, Q. Xue, *Sens. Actuators, B* **2016**, *225*, 233.
[11] Q. Kuang, C. Lao, L. W. Zhong, Z. Xie, L. Zheng, *J. Am. Chem. Soc.* **2007**, *129*, 6070.
[12] K. Katayama, H. Hasegawa, T. Noda, T. Akiba, H. Yanagida, *Sens. Actuators, B* **1990**, *2*, 143.
[13] P. M. Harrey, B. J. Ramsey, P. S. A. Evans, D. J. Harrison, *Sens. Actuators, B* **2002**, *87*, 226.
[14] H. Farahani, R. Wagiran, M. N. Hamidon, *Sensors* **2014**, *14*, 7881.
[15] T. Miyake, M. Rolandi, *J. Phys.: Condens. Matter* **2016**, *28*, 023001.
[16] N. Agmon, *Chem. Phys. Lett.* **1995**, *244*, 456.
[17] M. Gong, Y. Li, Y. Guo, X. Lv, X. Dou, *Sens. Actuators, B* **2018**, *262*, 350.
[18] H. Kähäri, P. Ramachandran, J. Juuti, H. Jantunen, *Int. J. Appl. Ceram. Technol.* **2017**, *14*, 50.
[19] W. Lin, C. Liao, T. Chang, S. Chen, R. Wu, *Sens. Actuators, B* **2015**, *209*, 555.
[20] V. Bondarenka, S. Grebinskij, S. Mickevieius, V. Volkov, G. Zacharova, *Sens. Actuators, B* **1995**, *28*, 227.
[21] B. Cheng, B. Tian, C. Xie, Y. Xiao, S. Lei, *J. Mater. Chem.* **2011**, *21*, 1907.
[22] J. Boudaden, M. Steinmabl, H. Endres, A. Drost, I. Eisele, C. Kutter, P. Muller-buschbaum, *Sensors* **2018**, *18*, 1516.
[23] X. Xiao, Q. J. Zhang, J. H. He, Q. F. Xu, H. Li, N. J. Li, D. Y. Chen, J. M. Lu, *Sens. Actuators, B* **2018**, *255*, 1147.
[24] Z. Zhen, Z. Li, X. Zhao, Y. Zhong, L. Zhang, Q. Chen, *Small* **2018**, *14*, 1703848.
[25] L. L. W. Chow, M. M. F. Yuen, P. C. H. Chan, A. T. Cheung, *Sens. Actuators, B* **2001**, *76*, 310.
[26] B. C. Yadav, R. Srivastava, C. D. Dwivedi, P. Pramanik, *Sens. Actuators, B* **2008**, *131*, 216.
[27] D. Zhang, X. Zong, Z. Wu, Y. Zhang, *Sens. Actuators, B* **2018**, *266*, 52.
[28] S. Kim, M. Y. Cho, I. S. Kim, W. J. Kim, S. H. Park, S. Baek, J. M. Oh, S. W. Kim, *Adv. Mater. Interfaces* **2019**, *6*, 1900359.
[29] Q. Ma, S. Huang, X. Wen, M. A. Green, A. W. Y. Ho-Baillie, *Adv. Energy Mater.* **2016**, *6*, 1502202.
[30] D. Zhou, D. Liu, G. Pan, X. Chen, D. Li, W. Xu, X. Bai, H. Song, *Adv. Mater.* **2017**, *29*, 1704149.
[31] C. Li, C. Han, Y. Zhang, Z. Zang, M. Wang, X. Tang, J. Du, *Sol. Energy Mater. Sol. Cells* **2017**, *172*, 341.
[32] T. Xuan, X. Yang, S. Lou, J. Huang, Y. Liu, J. Yu, H. Li, K. L. Wong, C. Wang, J. Wang, *Nanoscale* **2017**, *9*, 15286.
[33] L. Hu, G. Shao, T. Jiang, D. Li, X. Lv, H. Wang, X. Liu, H. Song, J. Tang, H. Liu, *ACS Appl. Mater. Interfaces* **2015**, *7*, 25113.
[34] K. Ren, L. Huang, S. Yue, S. Lu, K. Liu, M. Azam, Z. Wang, Z. Wei, S. Qu, Z. Wang, *J. Mater. Chem. C* **2017**, *5*, 2504.
[35] W. Xu, F. Li, Z. Cai, Y. Wang, F. Luo, X. Chen, *J. Mater. Chem. C* **2016**, *4*, 9651.
[36] Z. Weng, J. Qin, A. A. Umar, J. Wang, X. Zhang, H. Wang, X. Cui, X. Li, L. Zheng, Y. Zhan, *Adv. Funct. Mater.* **2019**, *1902234*.
[37] A. Rivadeneyra, J. Fernández-salmerón, M. Agudo, J. A. López-villanueva, L. F. Capitan-vallvey, A. J. Palma, *Sens. Actuators, B* **2014**, *195*, 123.
[38] J. Akedo, *J. Therm. Spray Technol.* **2008**, *17*, 181.
[39] J. Akedo, M. Lebedeb, *Jpn. J. Appl. Phys.* **1999**, *38*, 5397.
[40] J. Akedo, *J. Am. Ceram. Soc.* **2006**, *89*, 1834.
[41] E. S. Kim, J. G. Liang, C. Wang, M. Y. Cho, J. M. Oh, N. Y. Kim, *Sci. Rep.* **2019**, *9*, 680.
[42] J. J. Steele, M. T. Taschuk, M. J. Brett, *IEEE Sens. J.* **2008**, *8*, 1422.
[43] A. Alias, Z. Ahmad, A. B. Ismail, *Mater. Sci. Eng., B* **2011**, *176*, 799.
[44] A. Paxton, L. Thiên-Nga, *Phys. Rev. B* **1998**, *57*, 1579.
[45] A. M. M. Farea, S. Kumar, K. M. Batoo, A. Yousef, C. G. Lee, Alimuddin, *J. Alloys Compd.* **2009**, *469*, 451.
[46] S. Govinda, B. P. Kore, M. Bokdam, P. Mahale, A. Kumar, S. Pal, B. Bhattacharyya, J. Lahnsteiner, G. Kresse, C. Franchini, A. Pandey, D. D. Sarma, *J. Phys. Chem. Lett.* **2017**, *8*, 4113.
[47] M. Y. Cho, D. W. Lee, I. S. Kim, W. J. Kim, S. M. Koo, D. Lee, J. M. Oh, *Ceram. Int.* **2019**, *45*, 6702.
[48] Z. Chen, C. Lu, *Sensor Lett.* **2005**, *3*, 274.
[49] F. Huang, Y. Chen, T. Wu, *Nanotechnology* **2009**, *20*, 065501.
[50] H. Hong, D. Phan, G. Chung, *Sens. Actuators, B* **2012**, *171–172*, 1283.

[51] Q. Lin, Y. Li, M. Yang, *Sens. Actuators, B* **2012**, *161*, 967.
[52] M. M. Hawkeye, M. J. Brett, *Adv. Funct. Mater.* **2011**, *21*, 3652.
[53] A. Bearzotti, J. Mio, P. Innocenzi, P. Falcaro, E. Traversa, *J. Eur. Ceram. Soc.* **2004**, *24*, 1969.
[54] V. K. Tomer, S. Duhan, *Sens. Actuators, B* **2015**, *220*, 192.
[55] K. Jiang, H. Zhao, J. Dai, T. Fei, T. Zhang, *ACS Appl. Mater. Interfaces* **2016**, *8*, 25529.
[56] E. Raza, M. Asif, F. Aziz, M. Izzat, H. Ashraf, C. Teh, M. Ani, Q. Zafar, *Sens. Actuators, B* **2016**, *235*, 146.
[57] G. Banerjee, K. Sengupta, *Sens. Actuators, B* **2002**, *86*, 34.
[58] J. Zhao, Y. Liu, X. Li, G. Lu, L. You, X. Liang, F. Liu, T. Zhang, Y. Du, *Sens. Actuators, B* **2013**, *181*, 802.
[59] H. Wang, X. Zhang, Q. Wu, F. Cao, D. Yang, Y. Shang, Z. Ning, W. Zhang, W. Zheng, Y. Yan, S. V. Kershaw, L. Zhang, A. L. Rogach, X. Yang, *Nat. Commun.* **2019**, *10*, 1.
[60] B. Turedi, K. J. Lee, I. Dursun, B. Alamer, Z. Wu, E. Alarousu, O. F. Mohammed, N. Cho, O. M. Bakr, *J. Phys. Chem. C* **2018**, *122*, 14128.
[61] S. Agarwal, G. L. Sharma, *Sens. Actuators, B* **2002**, *85*, 205.
[62] Y. He, T. Zhang, W. Zheng, R. Wang, X. Liu, Y. Xia, J. Zhao, *Sens. Actuators, B* **2010**, *146*, 98.
[63] J. Yuk, T. Troczynski, *Sens. Actuators, B* **2003**, *94*, 290.
[64] M. Viviani, M. T. Buscaglia, V. Buscaglia, M. Leoni, P. Nanni, *J. Eur. Ceram. Soc.* **2001**, *21*, 1981.
[65] R. Wagiran, W. S. W. Zaki, S. B. M. Noor, A. H. Shaari, I. Ahmad, *Int. J. Eng. Technol.* **2005**, *2*, 22.
[66] S. H. Xiao, H. J. Xu, J. Hu, W. F. Jiang, X. J. Li, *Thin Solid Films* **2008**, *517*, 929.
[67] Y. Wu, Z. Gu, in *2009 Symp. on Photonics Optoelectronics* **2009**, 1, https://doi.org/10.1109/SOPO.2009.5230200.
[68] J. Wang, B. K. Xu, S. P. Ruan, S. P. Wang, *Mater. Chem. Phys.* **2003**, *78*, 746.
[69] B. Qiao, P. Song, J. Cao, S. Zhao, *Nanotechnology* **2017**, *28*, 445602.
[70] S. Lou, Z. Zhou, T. Xuan, H. Li, J. Jiao, H. Zhang, R. Gautier, J. Wang, *ACS Appl. Mater. Interfaces* **2019**, *11*, 24241.
[71] X. Zhang, B. Xu, J. Zhang, Y. Gao, Y. Zheng, K. Wang, *Adv. Funct. Mater.* **2016**, *26*, 4595.
[72] J. G. Liang, C. Wang, Z. Yao, M. Q. Liu, H. K. Kim, J. M. Oh, N. Y. Kim, *ACS Appl. Mater. Interfaces* **2018**, *10*, 851.
[73] J. G. Liang, E. S. Kim, C. Wang, M. Y. Cho, J. M. Oh, N. Y. Kim, *Sens. Actuators, B* **2018**, *265*, 632.
[74] C. Lee, M. Y. Cho, M. Kim, J. Jang, Y. Oh, K. Oh, S. Kim, B. Park, B. Kim, S. M. Koo, J. M. Oh, D. Lee, *Sci. Rep.* **2019**, *9*, 2166.